POLITECNICO DI TORINO
Repository ISTITUZIONALE

BLISK WITH SMALL GEOMETRY MISTUNING AND BLEND REPAIR: AS-MEASURED FE MODEL AND EXPERIMENTAL VERIFICATION

Original
BLISK WITH SMALL GEOMETRY MISTUNING AND BLEND REPAIR: AS-MEASURED FE MODEL AND EXPERIMENTAL VERIFICATION / Zhou, B., Zhao, J., Ye, N., Berruti, T.M.. - 8-B:(2022). (ASME Turbo Expo 2022: Turbomachinery Technical Conference and Exposition, GT 2022 Rotterdam, The Netherlands 2022) [10.1115/GT2022-82173].

Availability:
This version is available at: 11583/2974313 since: 2023-01-03T13:49:29Z

Publisher:
American Society of Mechanical Engineers (ASME)

Published
DOI:10.1115/GT2022-82173

Terms of use:

This article is made available under terms and conditions as specified in the corresponding bibliographic description in the repository

Publisher copyright
ASME postprint/Author's accepted manuscript

(Article begins on next page)

01 July 2026

BLISK WITH SMALL GEOMETRY MISTUNING AND BLEND REPAIR: AS-MEASURED FE MODEL AND EXPERIMENTAL VERIFICATION

Biao Zhou *
Jingchao Zhao
College of Energy and
Power Engineering
Nanjing University of Aeronautics
and Astronautics
Nanjing, 210016, China
Email: biao.zhou@nuaa.edu.cn

Nan Ye
College of Mechanical and
Electrical Engineering
Nanjing University of Aeronautics
and Astronautics
Nanjing, 210016, China
Email: yen@nuaa.edu.cn

Teresa M. Berruti
Dipartimento di Ingegneria Meccanica
e Aerospaziale
Politecnico di Torino
Torino,10129, Italy
Email: teresa.berruti@polito.it

ABSTRACT

This paper presents an 'As-Measured Model' of a blended blisk, built upon the measurement of the true geometry of the blisk by the 3D optical scanning technology. This high-fidelity model aims to account for the variances of blade frequencies and mode shapes within the real blisk in the presence of both the blend repair and inherent geometry mistuning due to manufacturing, etc. An improved mesh updating strategy is proposed to adapt a seed blisk finite element model to the measured geometry. The resultant 'as-measured model' is therefore able to accurately represent the measured blade-to-blade geometry variances. The classical blade detuning test in combination with a novel 'correction' procedure is employed to experimentally evaluate the 'blade-alone' frequency mistuning pattern in the real blisk. Experimental verification of the 'as-measured model' demonstrates that it is able to not only capture the 'blade-alone' frequency and mode shape variations due to both the blend and intrinsic blade geometry variances, but also to reproduce the global dynamics of the blended blisk with acceptable accuracy.

NOMENCLATURE

AMM As-Measured Model.
BDT Blade Detunign Test.
CBT Conventional Blade Test.
CI Coupling Index.
PC Point Cloud.
R Pearson correlation coefficient.

In this paper, the subscript '*i*' and '*j*' indicate variable.

1 INTRODUCTION

Blade integrated disks (blisks), extensively used in the fan/ compressor sections of advanced aeroengines, are vulnerable to inevitable blade damages in service like foreign object damages, etc. An efficient maintenance of the extremely expensive blisks requires that damaged blades can be cost-effectively repaired [1]. The 'blending' is a typical blade repair for small-sized damages where the damaged

---

[*] Address all correspondence to this author.

area is blended out. For minor damages not in the critical region of the blade, blend repair allows to minimize the stress concentration ratio at the damaged location and at the same time to maintain its functionality as much as possible.

Functional evaluation of the blended blisks is an indispensable step in the repair process in order to ensure its structural integrity and avoid failures not foreseen at the repair stage. Recently, there are increasing research interests that address the aerodynamic performance [2–4], aeroelastic behavior [5], fatigue strength [6] and ‘single’ blade vibration frequencies [7] of blended blisks. However, there is still a limited understanding of the blending effect on the global dynamics of blisks.

One of the primary challenge is to build a blended blisk model that is able to represent the structural dynamics of the real one-piece component with sufficient accuracy. This relies on the observation that small-sized blends may notably alter both the blade frequencies and mode shapes [8], adding further mistuning to a blisk with already intrinsic blade geometry variances caused by manufacturing tolerance and wear, etc [9]. Setting up blisk models of high accuracy is crucial for the prediction of forced response due to its susceptibility to geometric mistuning. Nevertheless, the traditional frequency-mistuning approaches, assuming a unique frequency mistuning source, fails to account for the changes in blade mode shapes due to geometry variance. Limited capability of the traditional blisk modeling methodologies therefore has been motivating the continuous researches in the modeling and analysis of geometrically mistuned blisks [10, 11].

There is a recent trend to capture the small blade-to-blade geometry variances, mainly due to manufacturing, through geometry measurements by a 3D optical scanning system [12, 13]. The measurement data in the form of point cloud is used to update the finite element model (FEM) of a nominal blisk, i.e., to project the blade surface nodes of the nominal FEM onto the measured point cloud. Therefore, blade geometric features could be explicitly modelled in the resultant ’as-manufactured model’ [14]. The updating process can be realized by specifically developed mesh morphing algorithms [15, 16] provided that the measured point cloud slightly deviate from the nominal FEM.

Experimental validation of the ’as-manufactured model’ of blisks is also of great interest. It is common practice to compare the blade mistuning evaluation results on the as-manufactured models with the experimentally identified mistuning pattern. Nonetheless, blade mistuning identification in a real blisk has been a longstanding and technically challenging issue due to the fact that mistuned blisks are rich dynamic structures with numerous closely spaced natural frequencies. For this reason, a traveling-wave excitation test rig has been used to perform multi-input modal tests so that the modal parameters of mistuned blisks could be better estimated. The blade mistuning was then identified by the well-known Fundamental Mistuning Model Identification method [17, 18]. However, the experimental campaign relying on the global response measurement on the whole blisk generally requires intensive efforts. Alternatively, the blade-by-blade measurement in conjunction with a detuning strategy (the term ’blade detuning test’ will be used throughout this paper) has been employed to determine the ’blade-alone’ mistuning of the entire blisk with relatively low experimental effort [19]. The key point is to temporarily attach identical detuning masses to all blades except the one being under test. The single blade, free of detuning mass, is then excited independently. Since the cyclic symmetry of the blisk is completely destroyed by the detuning masses, vibration would be largely confined in the individual blade under test and then ’blade-alone’ frequencies could be accordingly measured. The difference among the ’blade-alone’ frequencies of all the blades are quantified as blade mistuning pattern. Blade detuning tests are featured by its simple test setup and easy implementation. However, it should be pointed out that it is not truly possible to completely isolate the individual blade vibration from the entire blisk by mass detuning, due to the unavoidable inter-blade coupling. As highlighted in a recent research [20], the residual inter-blade coupling might give rise to inaccurate blade mistuning pattern through blade detuning tests.

Overall, the precedent researches turn out that as-manufactured models bring about improved mistuning evaluation capability for blisks with intrinsic blade geometry variance. This gives a strong incentive to perform an in-depth research on the high fidelity modeling and analysis for real blisks with both small blade geometry deviations and blend repairs. In particular, the extensive use of 3D optical scanning systems in the blisk repair process is also a major motivation for this research.

This paper presents an ‘As-Measured Model’ (AMM) of a blended blisk, built upon the measurements of the true geometry of the blisk by a 3D optical scanning system. An improved mesh updating strategy is developed to adapt the nominal blade mesh onto the as-measured geometry. Geometry mistuning due to both blends and intrinsic blade geometric variances can be effectively accounted for in this high-fidelity model. The capability of the AMM to represent the dynamics of the real blended blisk is experimentally verified by blade detuning tests and experimental modal tests. A novel mistuning identification method, recently developed by the authors [21], is here employed in order to improve the accuracy of the estimated mistuning pattern after the blade detuning tests. Comparison of the numerical predictions by AMM and experimental reference data is then fully addressed.

2 AS-MEASURED MODEL OF A BLENDED BLISK

This section presents the methodologies of constructing the ‘as-measured model’ of a blended blisk test piece (see Fig. 1). The blisk made of aluminium, consists of $N = 15$ downscaled, low-aspect-ratio blades on a disk with simplified geometry. This blisk was manufactured for academic research. The blade No.7 is purposefully blended with the blend shape depicted in Fig. 1.

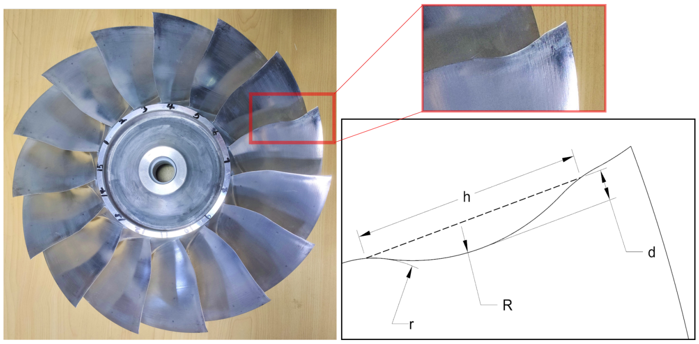

FIGURE 1: ACADEMIC BLISK, CLOSE-UP OF A SINGLE BLEND.

2.1 Geometry Measurement by 3D Optical Scanning

Blade-to-blade geometry variations in the blisk test piece are due to the blend, to the manufacturing tolerance and to the unexpected deformation occurring in the delivery process. A non-contact ATOS structured-blue-light 3D scanner is employed to acquire the blade surface geometry shape data by performing fringe projection scanning. It can be seen in Fig. 2a that a narrow band of blue light pattern is projected onto the surface of the test object. The fringe pattern will be geometrically distorted due the the surface shape of the object. The distorted pattern is then detected by two high-resolution cameras to produce the geometric contour of the blisk in the form of high-density point cloud.

A certain number of fringe projection scans had to be performed for the blisk test piece, due to its large size and complex cascade geometry. Since geometry mistuning mainly refers to the blade-to-blade geometry variance, the disk part inside the rim is not covered in the measured data. The individual point clouds are collected and merged into a unified point cloud of the blisk thanks to the standard reference circles distributed on the scanning surface. The blisk point cloud is then post-processed and converted into a triangulated surface mesh depicted in Fig. 2b.

The ATOS optical scanner allows for high resolutions down to 2.5μm. The measured blisk point cloud is thus sufficient to fully capture the small geometry variances among the blades.

2.2 As-Measured Model Construction

The blisk point cloud representing the measured geometry of the real one-piece component is used to construct the detailed FEM of the blended blisk. In previous research efforts, the mesh morphing strategies proved to be viable and valuable tools for semi-automatically generating a high-fidelity FEM directly from the blisk point cloud. On the contrary, the classical reverse engineering method tends to be time-consuming and less efficient because the point cloud data should be first processed into a CAD model to obtain the volumes, which are then meshed into a FEM.

Among the various state-of-the-art mesh morphing strategies, the common basis is to modify the blade surface node coordinates of an existing ‘seed’ FEM in order to better match the blisk point cloud. The bottom part of Fig. 3 presents the mesh updating scheme from the previous work [15]. A seed FEM with quadratic tetrahedral elements, usually coming from a nominal blisk design, serves as an initial approximation of the real component with blade geometry variations. The seed FEM is aligned with the point cloud in the same reference frame so that their locations and orientations pre-match as much as possible. In principle, the mesh updating scheme is achieved by projecting each individual surface node $N(x,y,z)$ of the ‘seed’ FEM along the vector $\vec{h}$, onto the plane determined by its 3 nearest neighboring vertices (v_1,v_2,v_3) in the point cloud. As a consequence, the surface mesh can be updated with the modified node coordinates $N^{'}(x',y',z')$ after the node projection procedure and the interior volume mesh will be regenerated accordingly.

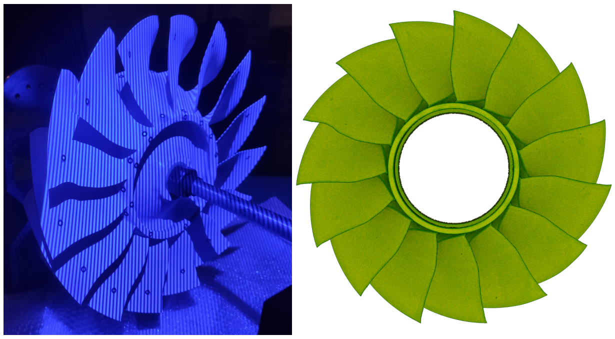

(a) fringe projection scan (b) blisk point cloud

FIGURE 2: OPTICAL GEOMETRY MEASUREMENT FOR THE BLENDED BLISK.

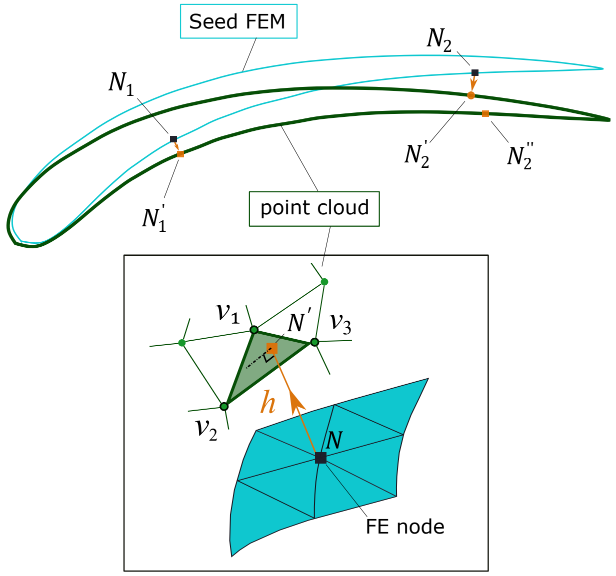

FIGURE 3: SCHEMATIC DIAGRAM OF THE ORIGINAL MESH UPDATING STRATEGY.

The original mesh updating scheme works smoothly provided that the FEM to PC (point cloud) distance is small, as indicated by the projection of node N_1 in the upper part of Fig. 3. This is usually proved to be a sufficient condition for the newly manufactured blisks. However, technical difficulty commonly arises for the large-sized blades experiencing geometric variations of relatively high magnitude. For instance, Fig. 3 depicts the potential projection problem of node N_2 near the trailing edge tip, where the local blade deformation exceeds the local blade thickness. By following the original mesh updating scheme, the seed FEM node N_2 on the pressure side will be automatically translated onto the closest point cloud on the suction side as an incorrect projected node N_2', whereas N_2'' should be the correct node projection on the pressure side of the blade point cloud.

An improved mesh updating strategy is therefore proposed to construct of the so-called ‘as-measured model’ of the blended blisk test piece. In essence, a ‘pre-morphing’ step for the seed FEM nodes is incorporated in order to override the potential problem of spurious node projection.

Improved Mesh Updating Strategy.

1. Prepare a seed FEM from the nominal design of the blisk test piece. Important considerations deserve special attention in this step: (1) the quadratic tetrahedral mesh should be of reasonable density so that it is able to not only meet the criterion of a conventional mesh study, but also potentially capture the small blade-to-blade geometric variances in the updating process; (2) the seed FEM of the non-blended sectors can be derived by replicating a base sector FEM, whereas for the blended sector, a seed FEM built upon a nominal blade with an approximated standard blend shape and geometry (see Fig. 1) is recommended. Otherwise, the updated FEM mesh could become warped or inverted around the blend.
2. Determine the reference surface for the next 'pre-morphing' step. The reference surface refers to one of the blade surfaces in the seed FEM, i.e., either the suction side or the pressure side, that practically deviates more from the measured blade PC. Hence, the reference face generally differs from blade to blade. As depicted in Fig. 4, the suction side of the seed FEM is set as the reference surface. The reference surface can be quantitatively determined by calculating the total amount of FEM node to PC distance for the suction side and pressure side, respectively. Given the large number of blade surface nodes (about $N_{\mathrm{FE}} \approx 2.7 \times 10^4$ nodes for one blade) and high-density point cloud ($N_{\mathrm{PC}} \approx 4.0 \times 10^6$ vertices for one blade), calculating the FEM node to PC distance by the conventional brute force computation is computationally expensive. Instead, the point cloud is used to build an efficient, indexed data structure, namely, the k-Dimensional tree. The nearest neighbour search algorithm is then employed to look up the 3 vertices in the tree that are nearest to any given FEM node as an input. In this way, the FEM node to PC distance can be rapidly obtained.
3. 'Pre-morphing' of the blade surface nodes of the seed FEM. Fig. 4 illustrates the step: (1) Each seed FEM node in the reference surface, e.g., N_1, is projected to its closest point cloud along the deformation vector $\vec{h}_1^{\mathrm{pre}}$ as N_1^{pre}. The implementation details of node projection will be elaborated in the next step. Note that this would be a correct node projection given that the reference surface is appropriately prescribed. (2) Search for the nearest neighboring node of N_1, as denoted by N_2 among the seed FEM blade surface nodes other than the reference surface, by employing the k-D tree and nearest neighbour search algorithm. (3) Impose the same deformation vector $\vec{h}_1^{\mathrm{pre}}$ to the node N_2 yields a pre-morphed node N_2^{pre}. This node is roughly close to, but not necessarily coincident with the point cloud of the non-reference surface.

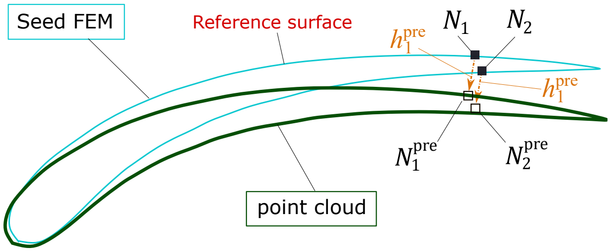

FIGURE 4: PRE-MORPHING STEP.

4. Project the pre-morphed nodes onto the point cloud. Since the pre-morphed nodes N_i^{pre} with $i = 1, 2, \ldots N_{\mathrm{FE}}$ approach the point cloud more than before, they will be translated to the correct position onto the point cloud by the node projection procedure depicted in Fig. 3: (1) for each pre-morphed node N_i^{pre}, query the 3 nearest neighboring vertices $(v_{i,1}, v_{i,2}, v_{i,3})$ in the point cloud by recalling the k-D tree established in Step 1; (2) calculate the coordinates of the projected node $N_i^{'}(x_i', y_i', z_i')$ on the closest triangulated surface mesh of the point cloud, as well as the deformation vector $\vec{h}_i$ representing the nodal displacement.
5. Nodal deformation vector alignment. This step is necessary to maintain sufficient mesh quality since the node projection procedure sometimes corrupts the surface elements due to improper aspect ratio, etc. The updated surface mesh of low quality might fail to regenerate the interior volume mesh subsequently. This is particularly true for the local blade surface areas featured by pronounced curvature.
   (1) Localize the invalid node projection. As shown in Fig. 5, one of the neighboring FEM nodes N_i is projected to $N_i^{'}$ via the vector $\vec{h}_i$. The seed FEM nodal distance between N and N_i is written as $\overline{NN_i}$. The deviation between the nodal deformation vectors $\vec{h}$ and $\vec{h}_i$ reads $\mathrm{d}\vec{h}_i = \vec{h} - \vec{h}_i$. Then a valid node projection is supposed to meet the criterion:

$$\left\| \mathrm{d}\vec{h}_i \right\|_2 \leq r \cdot \overline{NN_i} \tag{1}$$

where $\|\cdot\|_2$ stands for the Euclidean norm; r is a user-defined factor that limits the allowable relative node deformation.

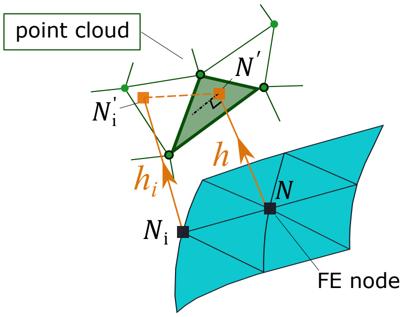

FIGURE 5: NODAL DEFORMATION VECTOR ALIGNMENT.

(2) Align the nodal deformation vector. The invalid node projection that does not satisfy the expression in Eqn. (1) is adjusted by substituting its vector $\vec{h}_i$ with

$$\vec{h}_a = \frac{1}{L}\Sigma_{j=1}^{L}\vec{h}_j \tag{2}$$

It indicates that the aligned nodal deformation vector of the seed FEM surface node N_i is the averaged deformation vector of its L nearest neighboring nodes. Note that both r and L could vary from blade to blade in the pursuit of well-deformed surface mesh of good quality.

6. Regenerate the interior tetrahedral volume mesh from the updated blade surface mesh.

The improved mesh updating strategy is implemented by a self-developed algorithm. Fig. 6 gives typical contour plots of the blade surface (including fillets) node to PC distance for the seed FEM before mesh updating and AMM afterwards. It is clearly seen that the proposed strategy works very well for both the non-blended blade 1 and blended blade 7. For the blade 1, in spite of the large blade deformation exceeding the local blade thickness around the leading edge tip, the proposed strategy manages to correctly project the seed FEM node to the points cloud. For the blended blade 7, the average FEM surface node to PC distance is reduced from 54μm to 0.92μm after mesh updating. Hence, the AMM is able to completely capture the measured blade-to-blade geometry variances with high-fidelity.

3 EXPERIMENTAL MISTUNING EVALUATION BASED ON BLADE DETUNING TESTS

This section is devoted to the blade detuning tests for the purpose of experimentally evaluating the frequency mistuning of the real blended blisk.

As shown later on, the inter-blade coupling of the blisk is one of the crucial factors that affect the mistuning evaluation results. For this reason, the inter-blade coupling strength of a nominal blisk is quantitatively examined by the ‘Coupling Index’ (CI), as illustrated in the frequency/ nodal diameter diagram in Fig. 7. Since the inter-blade coupling is governed by the blade-disk interaction in the blisk, the concept of CI relies on the observation of how the relative change of blade-alone frequency would affect the blade–disk modal frequencies [22,23]. The quantity of CI, ranging from 0% to 100%, indicates the mode-dependent inter-blade coupling strength. $\mathrm{CI} = 0\%$ represents a pure blade-alone mode with rigid disk, i.e, no inter-blade coupling exists. On the contrary, $\mathrm{CI} = 100\%$ corresponds to a disk mode with rigid blades. In reality, the variations of CI fall between the two extremes, and generally exhibit a strong dependence on the blade-dominant mode families. This research focuses on the 1st bending (1B) and 1st torsional (1T) blade-dominant mode families. An important remark is that the 1B mode family possesses stronger inter-blade coupling than the 1T mode family does.

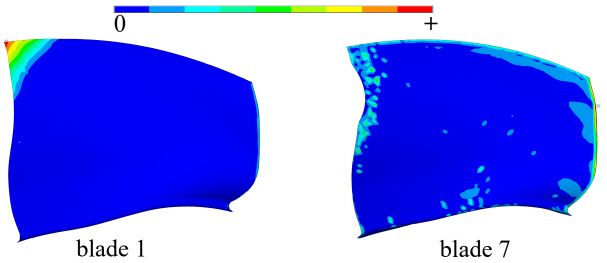

(a) before mesh updating

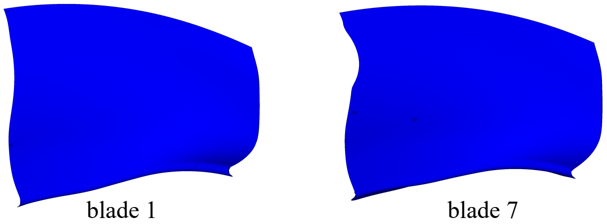

(b) after mesh updating

FIGURE 6: DEVIATION OF FEMS TO THE POINT CLOUD.

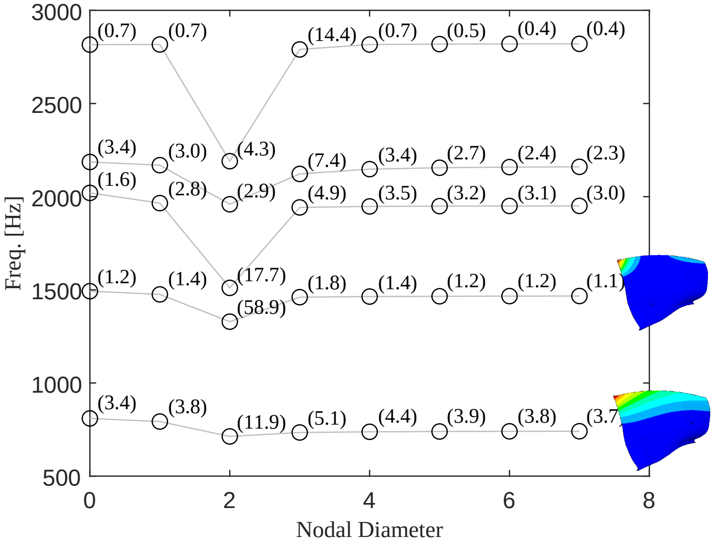

FIGURE 7: FREQUENCY VS. NODAL DIAMETER PLOT OF A NOMINAL BLISK WITH COUPLING INDICES.

3.1 Blade Detuning Test

The blade detuning test is performed for the blended blisk test piece in free support condition, as shown in Fig. 8a. Identical detuning masses, which consist of two magnetic cylinders attracting each other, are attached onto all the blades in the same position except the one currently under test. In Fig. 8b, the single blade without detuning mass is impulsively excited by a miniature impact hammer in a single point. A single test FRF is generated with the vibrational response around the leading edge tip measured at a single point by the non-contact Doppler laser vibrometer. Even if the blade-by-blade impact testing procedure is a well-established technique [24], practical considerations for a high-quality blade detuning test are emphasized as below:

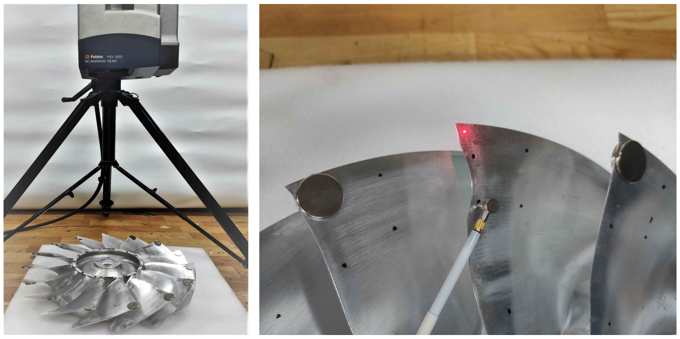

(a) test setup (b) excitation

FIGURE 8: BLADE DETUNING TEST.

1. Position and quantity of the detuning mass. It is definitely the governing factor of the mass detuning mechanism. This paper proposes to determine the detuning mass position by examining the modal kinetic energy density of a nominal blade. In principle, the location with the maximum kinetic energy density is recommended so that attaching the detuning mass will have the most impact on the target blade-alone modal frequency.
2. Location of the impulsive excitation. In practice, the test FRF quality also depends on the excitation location. It is often necessary to change its location for different target blade modes until smooth FRFs featured by prominent blade mode decoupling phenomena are produced.

The flat-shaped detuning mass ($m^d = 9.2\text{g}$) employed in this research on each blade has a relatively larger area, compared with the small-sized mass used in the previous blade detuning tests [21] for the same blisk test piece before blending. Its position around the leading edge tip enable it to cover the blade surface area with high kinetic energy density for both 1B and 1T blade modes. Covering with the detuning mass a larger area with high kinetic energy is expected to improve the quality of blade detuning test results.

Typical blade detuning test ('BDT') FRFs in the frequency range of 1B and 1T mode families are presented in Fig. 9. On the same plot the FRFs obtained by impact test on the blisk without any detuning mass are also depicted and marked as 'CBT' (conventional blade test). It can be seen that the CBT FRFs are characterized by clustered peaks due to the closely spaced blisk modes and blade mistuning effect. On the contrary, an isolated peak frequency $f_{m,i}^{\mathrm{T}}$ or $\omega_{m,i}^{\mathrm{T}}$ can be readily extracted from the BDT FRFs for the mth mode of the ith blade. This proves the capability of the detuning masses to decouple the blade-dominant mode families into individual blade modes.

BDTs allow to directly evaluate the mode-dependent blade mistuning pattern ${}^{f}\boldsymbol{\delta}_m^{\mathrm{bdt}} = [{}^{f}\delta_{m,1}^{\mathrm{bdt}}, \cdots, {}^{f}\delta_{m,N}^{\mathrm{bdt}}]^{\mathrm{T}}$ in terms of the mth target blade mode family as:

$$ {}^{f}\delta_{m,i}^{\mathrm{bdt}} = \frac{f_{m,i}^{\mathrm{T}} - \bar{f}_m^{\mathrm{T}}}{\bar{f}_m^{\mathrm{T}}} \tag{3} $$

where the preceding superscript ${}^{f}(\cdot)$ stands for the frequency mistuning pattern; $\bar{f}_m^{\mathrm{T}}$ is the mean value of the N isolated peak frequencies corresponding to the mth blade mode.

Alternatively, considering the general relation between the blade-alone frequencies and its elastic modulus as $f \propto \sqrt{E}$, the frequency mistuning pattern can be converted into an equivalent blade modulus mistuning pattern ${}^{E}\boldsymbol{\delta}_m^{\mathrm{bdt}}$ as:

$$ {}^{E}\delta_{m,i}^{\mathrm{bdt}} = 2\,{}^{f}\delta_{m,i}^{\mathrm{bdt}} + ({}^{f}\delta_{m,i}^{\mathrm{bdt}})^2 \tag{4} $$

where ${}^{E}(\cdot)$ stands for the modulus mistuning pattern.

An important remark is that the inter-blade coupling in the blisk can not be completely eliminated by detuning masses. The residual inter-blade coupling might imposes non-negligible impact on the isolated peaks of the BDT FRFs. Considerable residual inter-blade coupling effect can be observed due to the inadequacy of mass detuning mechanism, or when the target blade mode family exhibits strong blade-disk interaction.

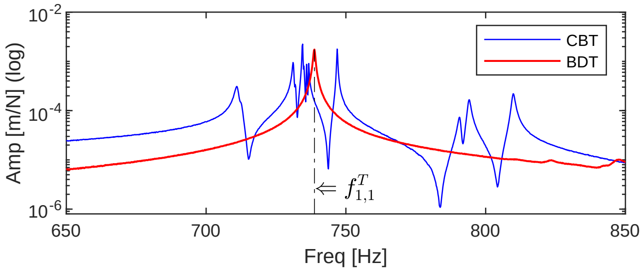

(a) around 1B mode family

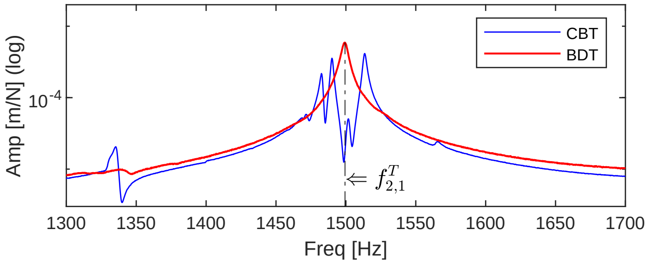

(b) around 1T mode family

FIGURE 9: COMPARISON OF TEST FRFS OF BLADE 1.

3.2 Mistuning Identification By Blade Detuning Test

After the BDTs, an additional 'correction' procedure was applied. This procedure was originally developed as a novel mistuning identification method in the authors' recent work [21]. Its primary intention is to quantify the residual inter-blade coupling due to mass detuning.

An assumed linear relationship representing the core of the 'correction' procedure is formulated as:

$$\frac{{\omega^{\mathrm{T}}_{m,i}}^{2} - \omega^{2}_{\mathrm{ref}}}{\omega^{2}_{\mathrm{ref}}} = \boldsymbol{\psi}^{\mathrm{T}} \cdot {}^{E}_{\mathrm{ref}}\boldsymbol{\delta}_m \tag{5}$$

where the left-hand side represents the test variation of the isolated peak frequency ${\omega^{\mathrm{T}}_{m,i}}^{2}$ for the mth mode of the ith blade with respect to a reference frequency $\omega^{2}_{\mathrm{ref}}$.

${}^{E}_{\mathrm{ref}}\boldsymbol{\delta}_m$ in the right-hand side denotes the 'true' blade modulus mistuning pattern to be identified for the mth blade mode. Note that the preceding subscript ${}_{\mathrm{ref}}(\cdot)$ implies that its reference should be consistent with ω_{ref}.

$\boldsymbol{\psi}$ is a N-dimensional influence coefficient vector quantifying the residual inter-blade coupling due to mass detuning, i.e., the influence of one blade's vibration on all the blades within the blisk. Its entries are centered around the ith blade as $\boldsymbol{\psi} = [\psi_l, \ldots, \psi_{-1}, \psi_0, \psi_1, \ldots, \psi_u]^{\mathrm{T}}$ in order to account for its cyclic nature. Namely, the ith entry of $\boldsymbol{\psi}$ is set as ψ_0, meanwhile ψ_{-1} and ψ_1 stand for the influence coefficients of the nearest neighboring blades in terms of the ith blade, etc. It turns out that $\boldsymbol{\psi}$ shows substantial dependence on the adequacy of mass detuning mechanism, as well as the dynamics of the blisk under test, e.g., the mode-dependent inter-blade coupling strength and the inherent blade mistuning. In particular, it will be shown later that ψ_0 can be seen as an indicator of the residual inter-blade coupling strength. In an ideal case where the detuning masses perfectly isolate the blades from one another and there is no residual coupling between the blades, $\boldsymbol{\psi}$ will have all zeros except for ψ_0=1.

In essence, Eqn. (5) mathematically bridges the gap between the variation of the isolated peak frequencies in the blade detuning test and the inherent blade mistuning of the blisk, by means of the residual inter-blade coupling effect. It can be potentially used for identifying the 'true' blade modulus mistuning pattern ${}^{E}_{\mathrm{ref}}\boldsymbol{\delta}_m$, provided that the influence coefficients in $\boldsymbol{\psi}$ are *a priori* known. Hence, the 'correction' procedure, or the novel mistuning identification method naturally boils down to a two-step scheme: (1) to approximate the unknown influence coefficients vector $\boldsymbol{\psi}$; (2) to identify the 'true' blade modulus mistuning pattern ${}^{E}_{\mathrm{ref}}\boldsymbol{\delta}_m$.

Step 1: Virtual Blade Detuning Test. The first step proposes to approximate the influence coefficients by numerically simulating a so-called virtual blade detuning test. It relies on a well-supported hypothesis that $\boldsymbol{\psi}({}^{E}\boldsymbol{\delta}^{\mathrm{bdt}}_m)$ closely approaches $\boldsymbol{\psi}({}^{E}_{\mathrm{ref}}\boldsymbol{\delta}_m)$, since the mistuning pattern ${}^{E}\boldsymbol{\delta}^{\mathrm{bdt}}_m$ experimentally derived in the realistic BDT is an approximation of the 'true' blade modulus mistuning pattern ${}^{E}_{\mathrm{ref}}\boldsymbol{\delta}_m$.

The virtual BDT starts from introducing a prescribed blade modulus mistuning pattern $\boldsymbol{\delta}^{\mathrm{V}} = {}^{E}\boldsymbol{\delta}^{\mathrm{bdt}}_m$, into a tuned blisk FEM. The superscript $(.)^{\mathrm{V}}$ indicates the virtual test. Similar to the realistic BDT, it is supposed to yield an isolated peak frequency $\omega^{\mathrm{V}}_{m,i}$ for the mth mode of the ith blade. At this point, Eqn. (5) for all the N blades in the virtual test are collected and rewritten as:

$$\begin{bmatrix} \frac{{\omega^{\mathrm{V}}_{m,1}}^2-\omega^2_{\mathrm{ref}}}{\omega^2_{\mathrm{ref}}} \\ \frac{{\omega^{\mathrm{V}}_{m,2}}^2-\omega^2_{\mathrm{ref}}}{\omega^2_{\mathrm{ref}}} \\ \vdots \\ \frac{{\omega^{\mathrm{V}}_{m,N}}^2-\omega^2_{\mathrm{ref}}}{\omega^2_{\mathrm{ref}}} \end{bmatrix} = \begin{bmatrix} \delta^{\mathrm{V}}_1 & \delta^{\mathrm{V}}_2 & \cdots & \delta^{\mathrm{V}}_N \\ \delta^{\mathrm{V}}_2 & \delta^{\mathrm{V}}_3 & \cdots & \delta^{\mathrm{V}}_1 \\ \vdots & \ddots & \ddots & \vdots \\ \delta^{\mathrm{V}}_N & \delta^{\mathrm{V}}_1 & \cdots & \delta^{\mathrm{V}}_{N-1} \end{bmatrix} \begin{bmatrix} \psi_0 \\ \psi_1 \\ \vdots \\ \psi_{-1} \end{bmatrix} = \boldsymbol{\Delta}\cdot\boldsymbol{\psi}({}^{E}\boldsymbol{\delta}^{\mathrm{bdt}}_m) \tag{6}$$

where $\boldsymbol{\Delta}$ is a circulant matrix that is composed of the known blade modulus mistuning values δ^{V}_i with $i = 1,2,\ldots N$. As a consequence, the influence coefficients in $\boldsymbol{\psi}({}^{E}\boldsymbol{\delta}^{\mathrm{bdt}}_m)$ can be sought by solving Eqn. (6).

Step 2: Blade Mistuning Identification. The second step is to identify the 'true' blade modulus mistuning pattern ${}^{E}_{\mathrm{ref}}\boldsymbol{\delta}_m$ by admitting that $\boldsymbol{\psi}({}^{E}_{\mathrm{ref}}\boldsymbol{\delta}_m) \approx \boldsymbol{\psi}({}^{E}\boldsymbol{\delta}^{\mathrm{bdt}}_m)$. Recall Eqn. (5) for all the N blades in the realistic blade detuning test and then re-organize them as:

$$\begin{bmatrix} \frac{{\omega^{\mathrm{T}}_{m,1}}^2-\omega^2_{\mathrm{ref}}}{\omega^2_{\mathrm{ref}}} \\ \frac{{\omega^{\mathrm{T}}_{m,2}}^2-\omega^2_{\mathrm{ref}}}{\omega^2_{\mathrm{ref}}} \\ \vdots \\ \frac{{\omega^{\mathrm{T}}_{m,N}}^2-\omega^2_{\mathrm{ref}}}{\omega^2_{\mathrm{ref}}} \end{bmatrix} = \begin{bmatrix} \psi_0 & \psi_1 & \cdots & \psi_{-1} \\ \psi_{-1} & \psi_0 & \cdots & \psi_{-2} \\ \vdots & \ddots & \ddots & \vdots \\ \psi_1 & \cdots & \psi_{-1} & \psi_0 \end{bmatrix} \begin{bmatrix} {}^{E}_{\mathrm{ref}}\delta_{m,1} \\ {}^{E}_{\mathrm{ref}}\delta_{m,2} \\ \vdots \\ {}^{E}_{\mathrm{ref}}\delta_{m,N} \end{bmatrix} = \boldsymbol{\Psi}\cdot {}^{E}_{\mathrm{ref}}\boldsymbol{\delta}_m \tag{7}$$

where $\boldsymbol{\Psi}$ is a circulant matrix that is composed of the influence coefficients in $\boldsymbol{\psi}({}^{E}\boldsymbol{\delta}^{\mathrm{bdt}}_m)$, which is numerically derived in Step 1.

${}^{E}_{\mathrm{ref}}\boldsymbol{\delta}_m$, which is also referenced to ω_{ref} previously prescribed in Eqn. (6) can be readily obtained by solving Eq. 7. In common practice, the identified blade modulus mistuning pattern will be transformed into ${}^{E}\boldsymbol{\delta}^{\mathrm{id}}_m$ or the equivalent frequency mistuning pattern ${}^{f}\boldsymbol{\delta}^{\mathrm{id}}_m$ with respect to a zero mean.

3.3 Experimental Mistuning Evaluation Results

The 'correction' procedure is applied to the realistic BDT results of the blended blisk. The equivalent blade modulus mistuning pattern ${}^{E}\boldsymbol{\delta}^{\mathrm{bdt}}_m$ directly evaluated from BDT FRFs is injected into a nominal blisk FEM to initiate the virtual BDT. Detuning masses are modeled as single-point mass elements. The locations of detuning masses, excitation and response measurements are consistent with the realistic test campaign. Instead of simulating the test FRFs by imposing an impulsive excitation, a harmonic analysis is performed by applying a harmonic forcing at the excitation point. This allows to produce harmonic response curves in a computational-efficient way. The well-isolated peaks can be immediately observed in the target frequency ranges. Identification results are presented in Fig. 10 and Fig. 11 for 1B blade mode and 1T blade mode, respectively.

The influence coefficients for the 1B mode are examined in Fig. 10a. The magnitude of ψ_i represents the extent to which one blade's vibration affects the neighboring blades in the BDT. ψ_0 exhibits the highest magnitude, i.e., the frequency variation of an isolated blade in the BDT principally depends on its inherent blade mistuning. While the adjacent blades also have minor influences with small-valued ψ_i ($i \neq 0$). It is reasonable to take the influence coefficient ψ_0 as an indicator of the residual inter-blade coupling strength and also as an indicator of the adequacy of the mass detuning mechanism. Note that $\psi_0 = 0.957$ for 1B mode in Fig. 10a has a magnitude close to 1, higher than that in the authors' previous work [21] (for 1B mode $\psi_0 = 0.871$ was derived from BDTs with smaller-sized detuning masses for the blisk test piece before blending). This implies that the position of the flat-shaped detuning mass is better selected and results in an improved mode decoupling performance. The residual inter-blade coupling for 1B mode is in fact negligible in the current BDT.

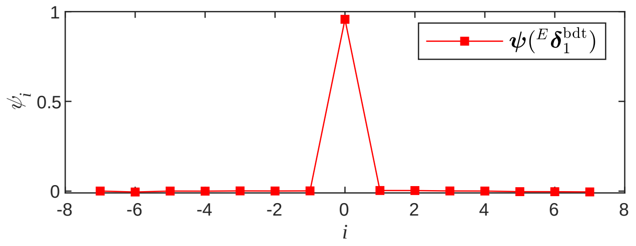

(a) influence coefficients

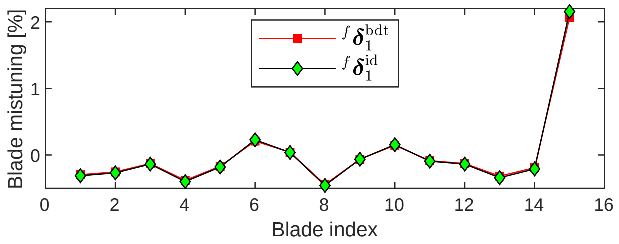

(b) blade mistuning pattern

FIGURE 10: MISTUNING EVALUATION RESULT-1B MODE

The directly evaluated frequency mistuning pattern $^{f}\boldsymbol{\delta}_1^{\mathrm{bdt}}$ is plotted in Fig. 10b. It can be seen that mistuning magnitudes of most blades fall in a narrow band, including the blended blade 7. Exception comes from the blade 15 with a high mistuning value up to 2.15%. The reason is that before the test, blade 15 has undergone unexpected geometric deflection in the tip area during delivery process, which is detectable by visual inspection. The correction procedure accounts for the residual inter-blade coupling and gives a corrected mistuning pattern as $^{f}\boldsymbol{\delta}_1^{\mathrm{id}}$. Nevertheless, a detectable improvement occurs only in the highly mistuned blade 15. The reason is that $\psi_0 = 0.957$ represents a high-level blade mode isolation, in this case already the BDT without corrections yields a good estimation of the true mistuning pattern for the 1B mode. On the contrary, in the previous work [21], $\psi_0 = 0.871$ indicated a not perfect isolation of 1B blade mode, in that case, the correction procedure to the BDT mistuning pattern had been effective.

Fig. 11a shows that the 1T blade mode is also highly isolated since $\psi_0 = 0.932$. As a consequence, the realistic BDT almost accurately captures the blade mistuning pattern by $^{f}\boldsymbol{\delta}_2^{\mathrm{bdt}}$. No significant improvement is observed in $^{f}\boldsymbol{\delta}_2^{\mathrm{id}}$ obtained after the correction procedure. This outcome is consistent with the finding in the the previous work [21]. An explanation is conceived from the viewpoint of inter-blade coupling. Since the 1T blade mode family is featured by a weaker inter-blade coupling than the 1B blade mode family (see Fig. 7), it gives a more favorable condition to decouple the blisk mode into a single blade mode by detuning masses. Therefore, the 'realisitc' BDT yields a fairly satisfactory estimation of the 'true' mistuning pattern for the 1T mode. Moreover, compared with the 1B blade mistuning pattern in Fig. 10b, the 1T blade mistuning values scatter in a much wider range. It implies that the 1T blade mode is more sensitive to the blade geometry variations than the 1B blade mode.

In the end of this section, the identified blade mistuning patterns are experimentally validated. On the one hand, the CBT results, i.e., the blade-by-blade impact test results for the blisk with all the detuning masses removed, is used as the experimental reference. As shown in Fig. 12, a complete collection of the CBT FRFs of all the N blades in gray definitely involve all the mistuned blisk modal

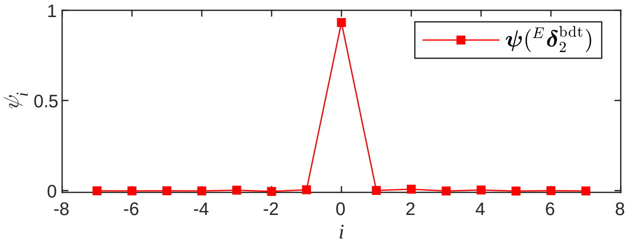

(a) influence coefficients

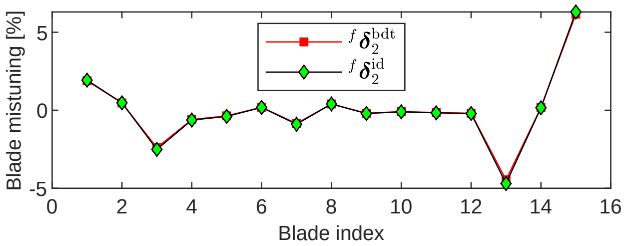

(b) blade mistuning pattern

FIGURE 11: MISTUNING EVALUATION RESULT-1T MODE

frequencies. On the other hand, the identified blade modulus mistuning patterns ${}^{E}\boldsymbol{\delta}_m^{\mathrm{id}}$ with $m = 1, 2$ are introduced into the nominal blisk FEM to compute the mistuned blisk modal frequencies in the range of 1B and 1T blade mode families, respectively. The computed modal frequencies are superimposed in Fig. 12 as a series of red dash-dot lines.

In general, excellent agreement can be seen between the peaks of the measured CBT FRFs and the numerically computed modal frequencies of the mistuned blisk. The comparison in Fig. 12 proves that, despite small discrepancies observed around 1330 Hz (corresponding to disk-dominant modes) and 1400Hz, the true ‘blade-alone’ mistuning pattern has been successfully identified with adequate accuracy.

4 EXPERIMENTAL VERIFICATION OF AS-MEASURED MODEL

This section aims to verify the prediction performance of the ‘as-measured model’ against the experimental reference data.

4.1 Blade Geometry Mistuning

The capability of the AMM to capture the blade geometry mistuning in the blended blisk test piece is firstly assessed. The identified ‘blade-alone’ frequency mistuning patterns ${}^{f}\boldsymbol{\delta}_m^{\mathrm{id}}$ with $m = 1, 2$ after the ‘correction’ procedure are considered as reliable experimental reference data. In the numerical aspect, blade-only AMMs (fillet included) are employed to obtain the corresponding ‘blade-alone’ modal frequencies. Modal analysis is performed for each isolated blade AMM with imposed root constraints. The cantilevered blade modal frequencies $f_{m,i}^{\mathrm{AMM}}$ of the ith blade are therefore used to calculate the numerically predicted frequency mistuning pattern ${}^{f}\boldsymbol{\delta}_m^{\mathrm{AMM}}$ in terms of the mth target blade mode:

$$ {}^{f}\delta_{m,i}^{\mathrm{AMM}} = \frac{f_{m,i}^{\mathrm{AMM}} - \bar{f}_m^{\mathrm{AMM}}}{\bar{f}_m^{\mathrm{AMM}}} \tag{8} $$

where $\bar{f}_m^{\mathrm{AMM}}$ is the mean value of the blade modal frequencies $f_{m,i}^{\mathrm{AMM}}$ with $i = 1, \cdots, N$.

The mesh density of the AMM is an important consideration during the experimental verification. In the author’s practice, the numerically predicted mistuning pattern ${}^{f}\boldsymbol{\delta}_m^{\mathrm{AMM}}$ is sensitive to the minor variation of the individual blade’s modal frequency $f_{m,i}^{\mathrm{AMM}}$, which is prone to node movement. A convergence study should be conducted to ensure the blade AMM mesh density is sufficient to

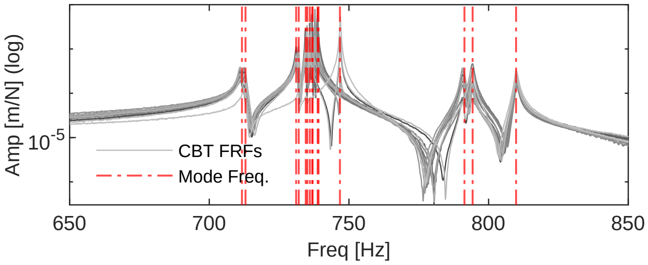

(a) 1B mode

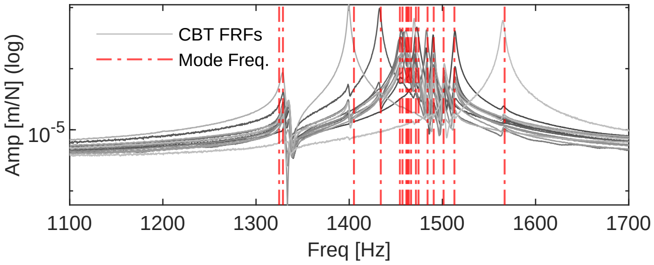

(b) 1T mode

FIGURE 12: COMPARISON OF CBT FRFS WITH SIMULATED BLISK MODAL FREQUENCIES

capture the frequency variations due to small blade geometric variations. In this research, there are about 3.48×10^5 nodes in the final blade AMM with a high mesh density.

Fig. 13 presents the ‘blade-alone’ frequencies and mode shapes predicted from the AMM. It can be seen that the 1B modal frequencies of a representative non-blended blade 1 and blended blade 7 are very close, whereas the 1T modal frequencies differ to a great extent partly because of the blend in blade 7. Meanwhile, it is graphically shown that the blend leads to significant variations for both the 1B and 1T mode shapes. However, due to the incompatible meshes between the non-blended and blended blades, the mode shape variances can not be further quantified by the traditional mode assurance criterion.

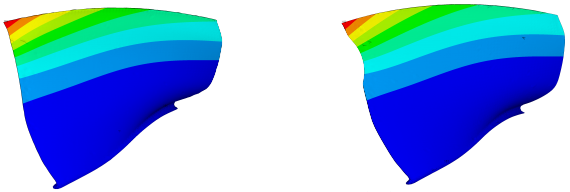

Blade1, 1B, 753.9Hz Blade7, 1B, 756.0Hz

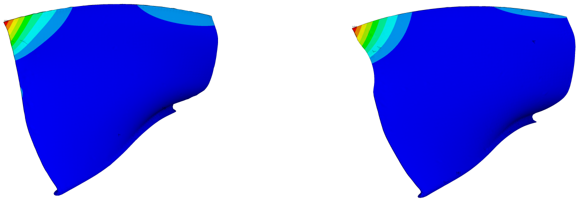

Blade1, 1T, 1549.3Hz Blade7, 1T, 1485.6Hz

FIGURE 13: ‘BLADE-ALONE’ FREQUENCIES AND MODE SHAPES

The experimentally identified mistuning pattern based on blade detuning tests and the numerically predicted mistuning pattern based on the AMM are compared in Fig. 14. The Pearson correlation coefficient R is employed to quantitatively measure the linear correlation between two mistuning patterns. It is supposed to be greater than 0, and close to 1, which would represent a perfect correlation. More specifically, Fig. 14a shows excellent correlation ($R = 0.983$) for the 1B mode between the numerically predicted and experimentally identified mistuning patterns. While there is relatively less , but still good correlation ($R = 0.940$) between the 1T blade mistuning patterns in Fig. 14b. The deviation could be partly attributed to the inadequate accuracy of the experimentally identified mistuning pattern ${}^{f}\boldsymbol{\delta}_2^{\mathrm{id}}$, as previously shown in Fig. 12b.

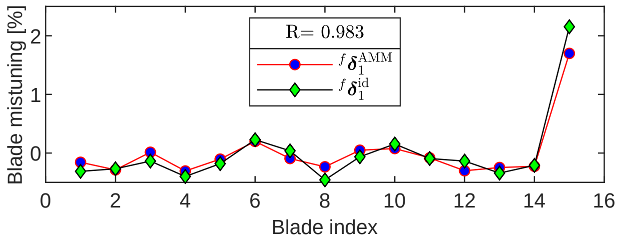

(a) 1B mode

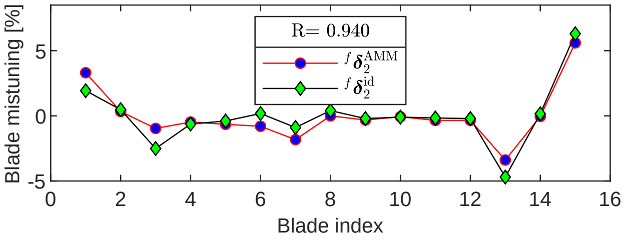

(b) 1T mode

FIGURE 14: COMPARISON OF MISTUNING PATTERNS

4.2 Global Dynamics of the Blended Blisk

A further attempt is made to demonstrate the capability of the AMM to reproduce the global dynamics of the blisk test piece. To this end, the standard single-input modal test has been carried out by employing an electromagnetic shaker exciting the blisk inside the disk rim. However, it turns out to be technically difficult to fully extract the mistuned blisk modes with a tight group of nearly repeated modal frequencies in the FRFs. From the numerical viewpoint, a modal analysis is performed for the AMM of the full blisk. This enables to compare the numerically computed and experimentally extracted mistuned blisk modal frequencies, as shown in Fig. 15. Some missing green square marks indicates that only a limited number of modal frequencies can be extracted. In spite of the incompleteness of the experimental modal test results, a good agreement between the two frequency curves is clearly observed. It should be reminded that in the AMM the central part of the blisk was not updated by the mesh updating strategy, but remains consistent with seed FEM generated from the nominal blisk design. This could be a potential reason for the modal frequency discrepancies in terms of each individual blisk mode.

Both the AMM and experimental modal test results enable to construct the representative blisk mode shapes by extracting the modal amplitudes in the axial direction (UZ) for the same point around each blade leading edge tip. Some typical blisk mode shapes are selected and compared in the normalized form, as depicted in Fig. 16. Some modes (see Mode 1 in both Fig. 16a and Fig. 16b) appear to be purely sinusoidal and the nodal diameters can be readily identified. While some other modes (see Mode 12 in both Fig. 16a and Mode 16 in Fig. 16b) are featured by significant vibration localization phenomena since certain blades exhibit relatively high modal amplitudes. Basically, the numerical blisk mode shapes predicted by AMM show good correlations with the counterparts determined experimentally. This proves that the AMM is able to predict the modal frequencies and mode shapes of the real blended blisk with acceptable accuracy.

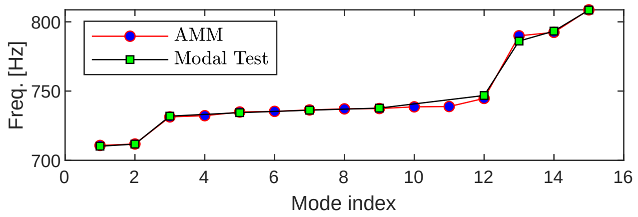

(a) 1B mode family

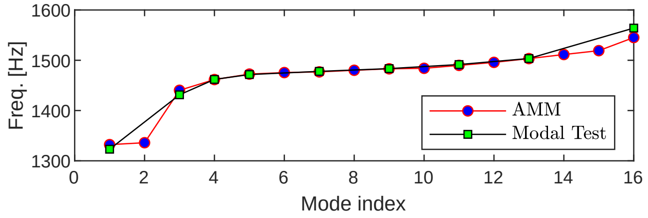

(b) 1T mode family

FIGURE 15: COMPARISON OF BLISK MODAL FREQ.

Overall, the good agreement in the correlation analysis reveals that geometric mistuning largely governs the blade mistuning pattern of the blended blisk. Benefiting from accurately capturing the measured blade-to-blade geometry variances, the AMM is able to not only fully account for the frequency and mode shape variations in the presence of both the blend and intrinsic blade geometry variances, but also to reproduce the global dynamics of the blended blisk as a whole. The remaining discrepancies between the experimental reference data and numerical predictions from the AMM could be linked to errors in the experimental campaign, uncertainties during the AMM construction and potential material variations within the blisk test piece.

5 CONCLUSIONS

This paper presents an 'as-measured model' of a blended blisk test piece, built upon the measured geometry by the 3D optical scanning system. The AMM aims to accurately model the variances of blade frequencies and mode shapes within the real blisk in the presence of both the blend repair and inherent geometry mistuning due to manufacturing tolerances, etc.

An improved mesh updating strategy is proposed to adapt a seed blisk FEM to the measured geometry. This strategy demonstrated to be suited to the AMM construction for large-sized blades experiencing geometric variations of high magnitude. The resultant AMM is able to explicitly represent the measured blade-to-blade geometry variances with high-fidelity.

The classical blade detuning tests in combination with a 'correction' procedure is employed to experimentally evaluate the frequency mistuning pattern in the real blisk. It was proved that the major factors that affect the performance of the experimental blade mistuning identification are twofold: (1) the mode-dependent inter-blade coupling strength of the blisk; (2) the residual inter-blade coupling strength due to mass detuning. The former is governed by the intrinsic dynamic characteristics of the blisk. The latter can be largely reduced by well-arranged detuning masses on the blades. The 'correction' procedure relies on the quantification of the residual inter-blade coupling and enables to evaluate the 'blade-alone' mistuning pattern with improved accuracy.

The prediction capability of the AMM was successfully verified in terms of the 'blade-alone' frequency mistuning patterns, as well as the modal frequencies and mode shapes of the full blisk. The general excellent agreement between the numerical predictions from the AMM and the experimental counterparts demonstrates that the AMM built upon the 3D optical geometry measurement could potentially be a viable tool for the vibration evaluation of blended blisks. A valuable benefit of the AMM is that it enables to disclose the mode shape variances due to both blend and inherent geometry mistuning, without assuming a unique frequency mistuning source, as in the traditional blisk modeling approach.

The obtained results are promising since they foresee the possibility of building a blisk AMM by 3D scanning technology to monitor the blisk's dynamic behaviour. This is of high engineering relevance, particularly considering that performing tests on a real blisk is technically difficult, time-consuming and requires intensive effort. This is also in line with the goal of the development of the

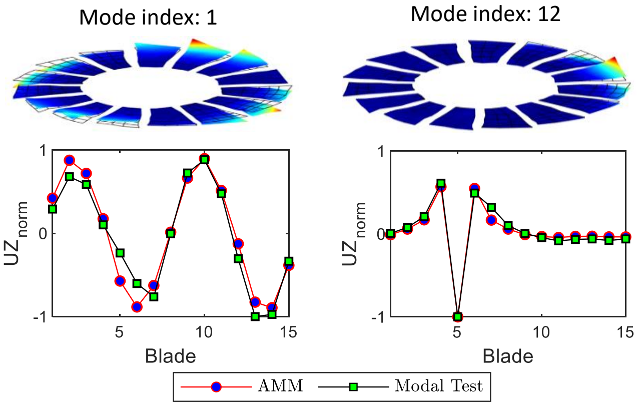

(a) 1B mode family

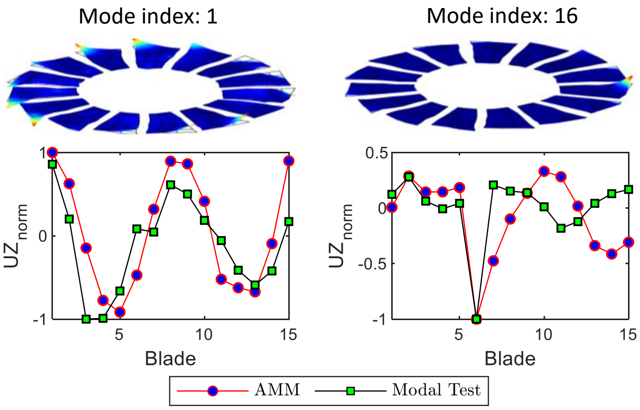

(b) 1T mode family

FIGURE 16: COMPARISON OF BLISK MODE SHAPES

leading-edge digital technology across the turbomachinery industry.

ACKNOWLEDGMENT

This project has received funding from the European Union's Horizon 2020 research and innovation programme under the Marie Sklodowska-Curie grant agreement No 891197. The blisk test piece under investigation is part of a project that has received funding from National Natural Science Foundation of China (Grant No. 52175098). This support is also gratefully acknowledged.

REFERENCES

[1] Aschenbruck, J., Adamczuk, R., and Seume, J. R., 2014. "Recent progress in turbine blade and compressor blisk regeneration". *Procedia CIRP,* ***22***, pp. 256–262.
[2] Keller, C., Kellersmann, A., Friedrichs, J., and Seume, J. R., 2017. "Influence of geometric imperfections on aerodynamic and aeroelastic behavior of a compressor blisk". In ASME Turbo Expo 2017: Turbomachinery Technical Conference and Exposition, p. V07BT36A007.
[3] Knapke, C. J., Wolff, M., and Johnston, D. A., 2019. "Blended fan blade effects on aerodynamic forces". In AIAA Scitech 2019 Forum, p. 1182.
[4] Knapke, C., Wolff, M., and Johnston, D. A., 2020. "Blended fan blade effects on unsteady aerodynamics". In AIAA Scitech 2020 Forum.

[5] Hanschke, B., Kühhorn, A., Schrape, S., and Giersch, T., 2019. “Consequences of borescope blending repairs on modern high pressure compressor blisk aeroelasticity”. *Journal of Turbomachinery,* ***141***(2), pp. 021002–7.

[6] Karger, K., and Bestle, D., 2015. “Parametric blending and fe-optimisation of a compressor blisk test case”. In *Advances in Evolutionary and Deterministic Methods for Design, Optimization and Control in Engineering and Sciences*, D. Greiner, B. Galván, J. Périaux, N. Gauger, K. Giannakoglou, and G. Winter, eds. Springer International Publishing, Cham, pp. 257–266.

[7] Berger, R., Häfele, J., Hofmeister, B., and Rolfes, R., 2018. “Blend repair shape optimization for damaged compressor blisks”. Advances in Structural and Multidisciplinary Optimization, Springer International Publishing, pp. 1631–1642.

[8] Brown, J. M., Kaszynski, A. A., Gillaugh, D. L., Carper, E. B., and Beck, J. A., 2020. “Optimization of airfoil blend limits with as-manufactured geometry finite element models”. In Turbo Expo: Power for Land, Sea, and Air, Vol. 84232, American Society of Mechanical Engineers, p. V011T30A029.

[9] Beck, J. A., Brown, J. M., Runyon, B., and Scott-Emuakpor, O. E., 2017. “Probabilistic study of integrally bladed rotor blends using geometric mistuning models”. In 58th AIAA/ASCE/AHS/ASC Structures, Structural Dynamics, and Materials Conference.

[10] Schnell, R., Lengyel-Kampmann, T., and Nicke, E., 2014. “On the impact of geometric variability on fan aerodynamic performance, unsteady blade row interaction, and its mechanical characteristics”. *Journal of Turbomachinery,* ***136***(9), pp. 091005–091005–14.

[11] Vishwakarma, V., Sinha, A., Bhartiya, Y., and Brown, J. M., 2015. “Modified modal domain analysis of a bladed rotor using coordinate measurement machine data on geometric mistuning”. *Journal of Engineering for Gas Turbines and Power,* ***137***(4), pp. 042502–042502–8.

[12] Schoenenborn, H., Grossmann, D., Satzger, W., and Zisik, H., 2009. “Determination of blade-alone frequencies of a blisk for mistuning analysis based on optical measurements”. In ASME Turbo Expo 2009: Power for Land, Sea, and Air, pp. 221–229.

[13] Popig, F., Hönisch, P., and Kühhorn, A., 2015. “Experimental and numerical analysis of geometrical induced mistuning”. In Turbo Expo: Power for Land, Sea, and Air, Vol. 56772, American Society of Mechanical Engineers, p. V07BT32A024.

[14] Kaszynski, A. A., Beck, J. A., and Brown, J. M., 2014. “Automated finite element model mesh updating scheme applicable to mistuning analysis”. p. V07BT33A025.

[15] Maywald, T., Backhaus, T., Schrape, S., and Kühhorn, A., 2017. “Geometric model update of blisks and its experimental validation for a wide frequency range”. In ASME Turbo Expo 2017: Turbomachinery Technical Conference and Exposition, p. V07AT30A001.

[16] Carassale, L., Bruzzone, S., Cavicchi, A., and Marrè Brunenghi, M., 2018. “Representation and analysis of geometric uncertainties in rotor blades”. In ASME Turbo Expo 2018: Turbomachinery Technical Conference and Exposition, p. V07CT35A025.

[17] Kaszynski, A., Brown, J., and Beck, J., 2015. “Experimental validation of an optically measured geometric mistuning model using a system id approach”. In 17th AIAA Non-Deterministic Approaches Conference.

[18] Gillaugh, D. L., Kaszynski, A. A., Brown, J. M., Beck, J. A., and Slater, J. C., 2019. “Mistuning evaluation comparison via as-manufactured models, traveling wave excitation, and compressor rigs”. *Journal of Engineering for Gas Turbines and Power,* ***141***(6).

[19] Beirow, B., Kühhorn, A., Figaschewsky, F., Hönisch, P., Giersch, T., and Schrape, S., 2019. “Model update and validation of a mistuned high-pressure compressor blisk”. *The Aeronautical Journal,* ***123***(1260), pp. 230–247.

[20] Lupini, A., Shim, J., Callan, S., and Epureanu, B. I., 2021. “Mistuning identification technique based on blisk detuning”. *AIAA Journal*, pp. 1–9.

[21] Zhou, B., Zhao, J., and Berruti, T., 2021. “Exploration of blade detuning tests for mistuning identification of blisks”. *Mechanical Systems and Signal Processing*, p. In major revision.

[22] Avalos, J., and Mignolet, M. P., 2010. “On damping entire bladed disks through dampers on only a few blades”. *Journal of Engineering for Gas Turbines and Power,* ***132***(9), pp. 092503–10.

[23] Zhou, B., Thouverez, F., and Lenoir, D., 2014. “Essentially nonlinear piezoelectric shunt circuits applied to mistuned bladed disks”. *Journal of Sound and Vibration,* ***333***(9), pp. 2520–2542.

[24] Kuehhorn, A., and Beirow, B., U.S. Patent 12078608, Sep. 2011. Method for determining blade mistuning on integrally manufactured rotor wheels.